A profile monitor for proton radiography experiments at the Los Alamos Neutron Science Center

Morris, Christopher; O'Brien, Lauren Nicole; Bruhaug, Gerrit Manfred Erich; Danielson, Jeremy; Farmer, Skylar Nicole; Fensin, Saryu Jindal; Freeman, Matthew Stouten; Fresquez, Matthew; Hall, Andrew Lawrence; Llobet Megias, Anna; Mariam, Fesseha Gebre; Martinez, Israel F.; Mavis, Erin Elizabeth; Medina, Jason Jerry; Meijer, William Zachary; Neukirch, Levi Patrick; Sandoval, Steven Joseph; Sandstrom, Mary M.; Schmidt, John Louis IV; Smith, Erick; Tang, Zhaowen; et al.

To be published in: Review of Scientific Instruments

DOI to publisher's version: 10.1063/5.0251430

Review of Scientific Instruments

RESEARCH ARTICLE | MAY 29 2025

A profile monitor for proton radiography experiments at the Los Alamos Neutron Science Center

Lauren O'Brien ✉ ; Gerrit Bruhaug ; Jeremy Danielson ; Skylar Farmer ; Saryu Fensin ; Matt Freeman ; Matthew Fresquez; Drew Hall; Anna Llobet ; Fesseha Mariam ; Israel Martinez ; Erin Mavis; Jason Medina; Wil Meijer ; Levi Neukirch ; Steven Sandoval ; Mary Sandstrom; John Schmidt, IV ; Erick Smith ; Zhaowen Tang ; Carl Trujillo ; James Wernicke ; Brandon White ; Christopher L. Morris

Rev. Sci. Instrum. 96, 053303 (2025)
https://doi.org/10.1063/5.0251430

AIP Publishing

Review of Scientific Instruments ARTICLE pubs.aip.org/aip/rsi

A profile monitor for proton radiography experiments at the Los Alamos Neutron Science Center

Cite as: Rev. Sci. Instrum. 96, 053303 (2025); doi: 10.1063/5.0251430
Submitted: 2 December 2024 • Accepted: 26 April 2025 •
Published Online: 29 May 2025

Lauren O'Brien,[a] Gerrit Bruhaug, Jeremy Danielson, Skylar Farmer, Saryu Fensin, Matt Freeman, Matthew Fresquez, Drew Hall, Anna Llobet, Fesseha Mariam, Israel Martinez, Erin Mavis, Jason Medina, Wil Meijer, Levi Neukirch, Steven Sandoval, Mary Sandstrom, John Schmidt IV, Erick Smith, Zhaowen Tang, Carl Trujillo, James Wernicke, Brandon White, and Christopher L. Morris

AFFILIATIONS

Los Alamos National Laboratory, Los Alamos, New Mexico 81745, USA

[a]**Author to whom correspondence should be addressed:** lobrien@lanl.gov

ABSTRACT

The Proton Radiography (pRad) facility at the Los Alamos Neutron Science Center utilizes pulses of protons delivered by the 800 MeV linear accelerator to produce a series of radiographic images to study the dynamic behavior of materials under extreme conditions. Radiographs taken with an empty field of view, or beam pictures, are used to normalize transmission. However, because the center of the proton beam shifts between pulses, an in situ method for measuring beam position is required to normalize images for beam movement to perform absolute radiography. The beam profile monitor described here uses an array of scintillating fibers positioned in the beam path to produce light proportional to beam intensity across the beam cross section. This light is detected using fast photodiodes and a digital oscilloscope, providing a response time of several nanoseconds—suitable for measuring the 50-ns proton pulses used in pRad. The profile monitor achieves a measured position precision of 40 μm and an intensity precision of 0.7%, allowing for beam movement corrections to be applied to images, thereby improving data accuracy and image quality.

I. INTRODUCTION

The Proton Radiography (pRad) facility at the Los Alamos Neutron Science Center (LANSCE) utilizes an 800 MeV proton beam from a linear accelerator to generate a series of radiographic images, enabling the study of dynamic material behavior in high-explosive-driven experiments.[1–4] These radiographs provide valuable insights into the areal density of the object of interest—which varies from experiment to experiment—and how it evolves throughout the dynamic process by extracting transmission data from the images.[5–10] To obtain accurate transmission data, the shape of the incident beam must be accounted for by normalizing each radiograph with the beam shape at the time of image acquisition. The proton beam shape is well described by a 2D Gaussian, but the center of this Gaussian shifts from pulse to pulse.

Previously, image detectors upstream of the object have been used to correct for beam motion, but they could not be used for multiple pulses due to their slow response.[11] Before the deployment of the beam profile monitor, these beam shifts were corrected using a two-step process. First, images were normalized by an average beam image. Then, 2D polynomials were fit to the edges of the ratio outside the region of interest, and the ratios were divided by the fitted polynomial in a process known as "flattening". However, this approach is not always feasible, as some experiments involve objects that completely fill the field of view, making beam regions outside of the region of interest inaccessible for measurement.

The beam profile monitor provides a direct method for measuring the beam Gaussian in each image. This capability ensures accurate beam shape characterization even when the object occupies the entire field of view, eliminating the need for flattening. In

this paper, we present a beam profile monitor and analysis method designed to correct pRad transmission data for pulse-to-pulse fluctuations in beam position and intensity in high-explosive-driven experiments.

II. BACKGROUND

pRad experiments primarily focus on understanding the response of various materials to high-explosive-driven shocks. The configuration of the proton radiography system varies depending on the required field of view dimensions for a given experiment, with three available magnification settings: ×1, ×3, and ×7. The ×3 magnification configuration—used for the data presented in this paper—is shown in Fig. 1. This setup consists of a matching section followed by two imaging lenses.[12]

The illuminating beam is formed using a tantalum sheet to induce Coulomb multiple scattering,[13] followed by a drift section and a set of matching quadrupole magnets. These magnets generate an angle–position correlation in the beam, which cancels first-order chromatic aberrations in the lens system.[12] The imaging system includes two quadruplet lenses: the first transfers the beam to the object location, while the second forms images of protons transmitted through the object. For the experimental data presented here, the second lens functioned as a magnifier.

The accelerator beam is chopped into multiple pulses, each used to capture an image, covering a total time range of up to 0.625 ms. The imaging system currently consists of seven three-frame cameras,[14] enabling the capture of 21 dynamic frames per experiment.

Radiographs obtained at pRad provide information on the transmission and areal density of the object throughout the dynamic experiment. The calculations used to extract this information will be discussed in detail later in this paper.

III. PROFILE MONITOR DESIGN

The profile monitor was constructed by securing 1 mm diameter Saint-Gobain BCF-12 scintillating fibers into an array of slots in a 3D-printed frame using epoxy, as shown in Fig. 2. When the beam passes through the monitor, the fibers produce light, which is transported 15 m via 1 mm diameter transport fibers to a 0.8 mm^2 Thorlabs SM05PD2B photodiode, selected for its 1.0 ns response

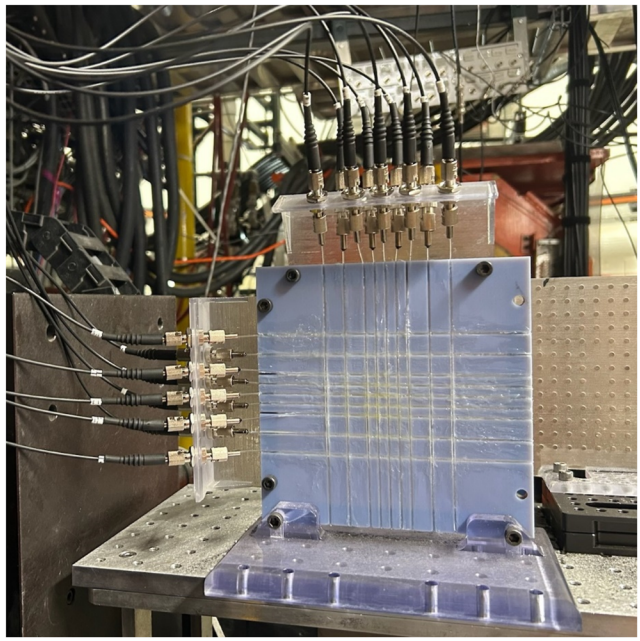

FIG. 2. Photograph of the profile monitor.

time. The transport fibers were introduced to mitigate noise interference caused by the capacitance discharge unit used to initiate the high explosives. Before their implementation, when photodiodes were directly attached to the monitor and signals were transmitted via coaxial cables, high-voltage noise obscured the signals during dynamic experiments.

Unconditioned signals from four photodiodes were recorded using two 1 GHz, 8-bit digital oscilloscopes for each axis (x and y), resulting in a total of eight oscilloscope traces per beam pulse. Each experiment utilizes eight fibers out of the 18 available, as each oscilloscope accommodates four inputs. This setup provides sufficient spatial resolution while minimizing physical space requirements and financial costs associated with additional oscilloscopes. The 18-fiber design allows for variable configurations with different spacing options—2.54, 1.27, and 0.60 cm spacing—corresponding

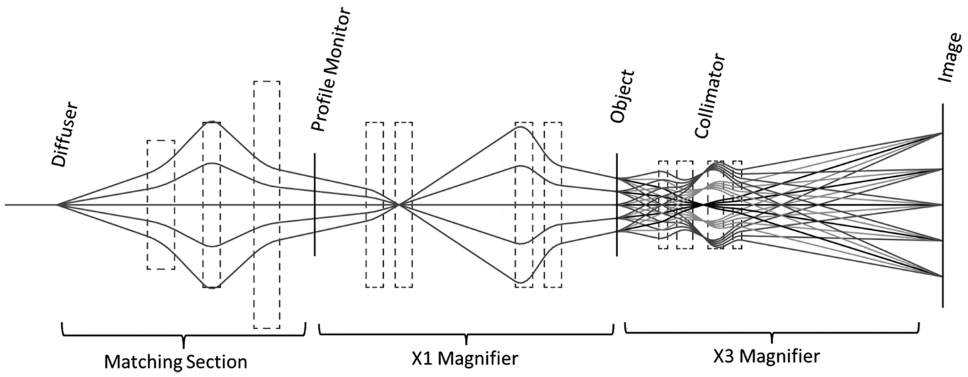

FIG. 1. Schematic of the imaging system. The beam from the left passes through a tantalum diffuser, a set of quadrupole magnets to produce an angle–position correlation in the beam, a lens to transport the beam to the object, and another lens to image the object on the scintillator plate. The lens used here was a times three magnifier (×3).

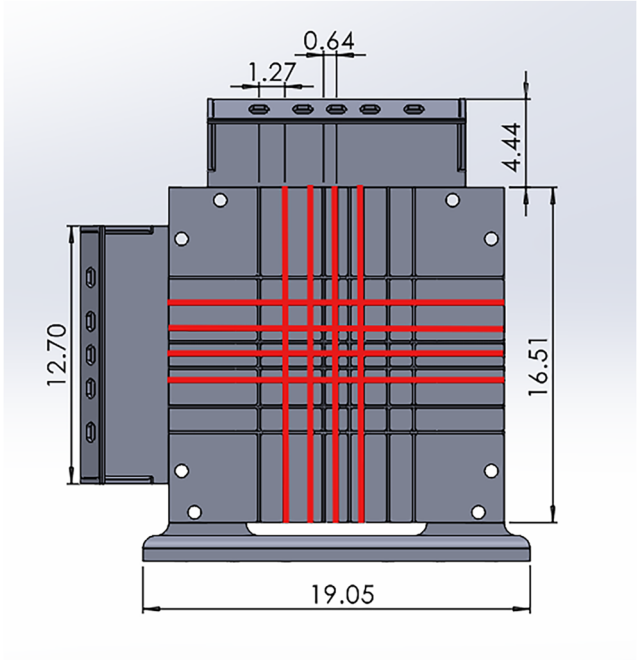

FIG. 3. Screenshot of the SolidWorks 3D model of the profile monitor with dimensions in centimeters. The grid pattern is the same on the x and y axes. The highlighted fibers indicate the fibers used in the experimental data presented in this paper. The fibers have a 1.27 cm spacing as shown in the image, giving a total area monitored of 3.81 × 3.81 cm.

to the three pRad magnifications. The specific fibers used in the data presented in this paper are indicated in Fig. 3.

An analysis process was developed for the beam profile monitor and integrated into the existing image analysis framework used at pRad. To demonstrate the monitor's effectiveness in normalizing transmission during a dynamic experiment, we use a representative pRad experiment, pRad0942. This experiment was designed to investigate the impact of a surface defect on a metal target, specifically its effects on shock propagation and surface damage. Sections IV–VI will outline the analysis procedure in detail.

IV. IMAGE ANALYSIS PROCESS

Sections IV A–IV B will outline the standard image analysis process at pRad and demonstrate how beam position data from the profile monitor are incorporated into this process, specifically in the "flattening" step of the standard analysis procedure. The following are several types of images acquired for the experiment, which will be referenced throughout this analysis:

- Dark-field images: captured with no beam to account for ambient room light background.
- Beam images: taken without an object at the object location.
- Static images: acquired with the object installed and aligned before the dynamic experiment.
- Dynamic images: collected during the experiment itself.

A. Dark current correction

The first step in image analysis is correcting for dark current in the cameras, the dark current correction. Typically, ten dark-field images are taken and averaged. Each dynamic image is then corrected by subtracting this averaged dark-field image to remove background noise.

B. Fixed pattern correction

After background correction, the processed images are used to generate fixed pattern corrections specific to each camera. After passing through the diffuser, the beam is transported to the first image plane, where fixed pattern noise—arising from the scintillator and camera—must be removed. The beam shape is primarily determined by multiple Coulomb scattering in the diffuser and is best modeled as a 2D Gaussian. Fixed pattern images are obtained by fitting a 2D Gaussian [Eq. (1)] to the processed beam images and saving the ratio of this fit as the fixed pattern correction (Fig. 4),

$$N(x,y) = S\frac{dxdy}{2\pi\sigma_x\sigma_y}e^{\frac{(x-x_0)^2}{2\sigma_x^2}+\frac{(y-y_0)^2}{2\sigma_y^2}}. \quad (1)$$

Here, $N(x,y)$ is the image, σ_x, σ_y and x_0, y_0 are the beam width and center in the x and y directions, respectively, and S is the integral of the image. The widths were fixed at their average values, and the centers and integral were fitted.

The static and dynamic images are divided by these fixed pattern images to remove the fixed pattern structure as shown in Fig. 5.

C. Calibration to a common object coordinate system

Next, the dynamic images must be calibrated to a common set of object coordinates. This calibration is performed using a fiducial plate placed at the object location. The fiducial plate contains a known pattern of tungsten rods, and the positioning of these rods in each camera's image allows for the transformation from object plane coordinates to each camera's coordinate system to be determined. The objective is to map all seven unique camera perspectives onto a unified object coordinate system, ensuring that all 21 frames are properly aligned.

D. Beam shape correction

The final step in the image analysis process is to remove the beam shape from the images and is the step of the analysis that the profile monitor greatly improves. Prior to the addition of the profile monitor, this step was done using a method called "flattening," which was described in the introduction. Profile monitor data is used to determine the x-centroid (x_0), y-centroid (y_0), and integral, S, of the incident beam for each dynamic image. These parameters are then used to calculate a 2D Gaussian, by which each processed image is divided to produce the final normalized transmission image, $T(x,y)$ (Fig. 6).

V. PROFILE MONITOR ANALYSIS

A. Calibration

Before the profile monitor data can be used in the image analysis process, the channels must be calibrated, as the light output

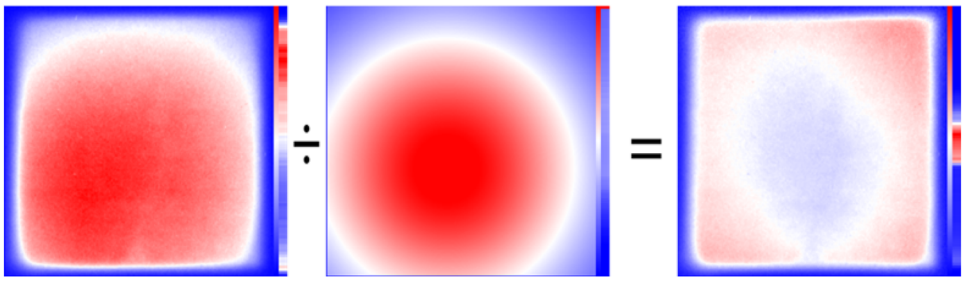

FIG. 4. Process of calculating the fixed pattern correction. From left to right: the uncorrected image, 2D Gaussian, and the fixed pattern correction. The color scales for each image are shown in the bar on the right of each image.

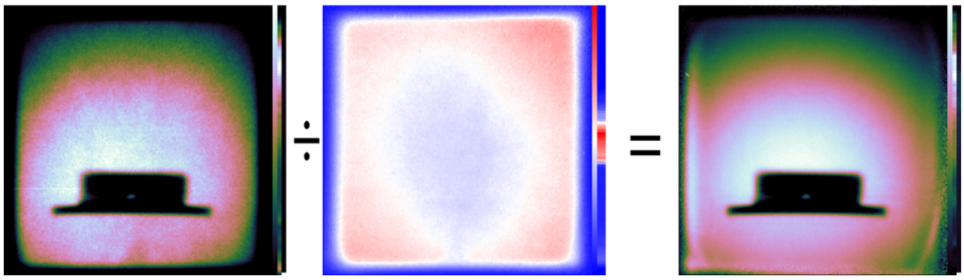

FIG. 5. Applying the fixed pattern correction to a static image. From left to right: the background-corrected static image, the fixed pattern correction, and the fixed pattern-corrected static image. The significant reduction in image graininess—caused by the fixed pattern structure in the scintillator—is clearly visible in the final corrected image on the right.

from the eight channels used varied by a factor of 20, as shown in Fig. 8. Some channels exhibited significant light loss due to fiber and cladding damage, which can be visually observed as light leakage near the top of the illuminated fiber in Fig. 7.

The sensitivity of each channel was determined by normalizing the profile monitor channels to a Gaussian, whose width was measured using spatially calibrated beam images. The profile monitor was then calibrated using eight sets of beam images from each of the 21 camera images, resulting in a total of 168 images with corresponding profile monitor data, as shown in Fig. 8.

The measured sensitivities for each channel were used to analyze the data from each pulse for all the static, dynamic, and beam images.

B. Obtaining beam position

A plot of the sensitivity corrected profile monitor data for a typical run is shown in Fig. 9. The vertical gray lines show integration gates corresponding to each camera picture pulse. The system time resolution was observed to be about 6 ns (after the transport fiber) with a noticeable 1 μs tail with an integrated area of 3% of the signal. A baseline and a tail correction (dashed lines) were applied to each of the traces.

The voltage traces were integrated across each of the camera gates corresponding to timing for each image, obtaining intensity measurements for each channel for each image. Then, a Gaussian was fit to the four resulting intensity values in the x and y directions to obtain the profile monitor centroid and amplitude. The centroids and amplitudes from the beam profile monitor data were fit to centroids and amplitudes from the beam images using linear regression. The results allow for the prediction of beam position and amplitude from profile monitor data alone. All the images can be divided by the predicted beam images obtained from the profile monitor data, as shown in Fig. 6, eliminating the need for "flattening".

C. Profile monitor precision

To assess the precision of the profile monitor, the predicted beam positions obtained from the profile monitor data were compared to the measured beam positions from beam images. A linear fit was performed between the beam centroids and amplitudes measured from the profile monitor data and those from the beam images,

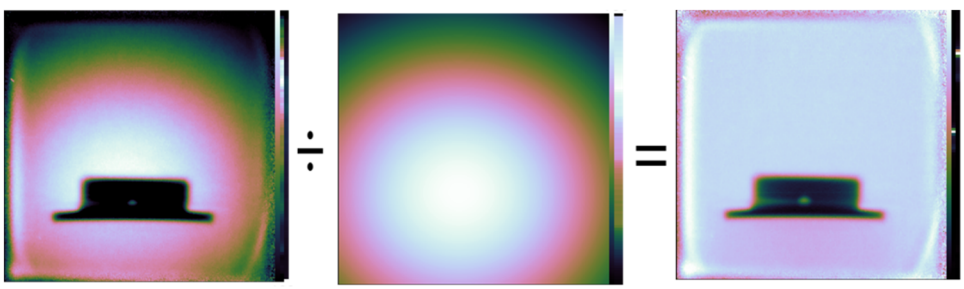

FIG. 6. Flattening procedure using the profile monitor data for the dynamic image from camera T. From left to right: the processed image containing the beam shape, the beam shape for this frame from the profile monitor data, and the image after dividing by the beam shape. The absence of the shape of the beam can be clearly observed in the final product.

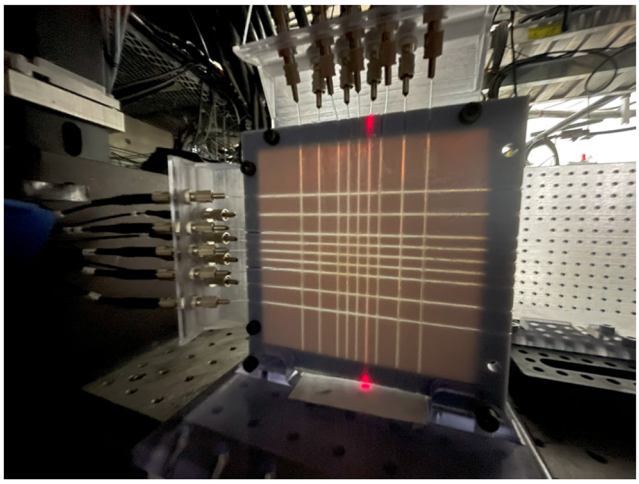

FIG. 7. Some light leakage can be observed near the top of the fiber indicating damage to the fiber, which was determined to be the source of signal intensity inconsistencies between channels. Future improvements to the profile monitor aim to address this problem.

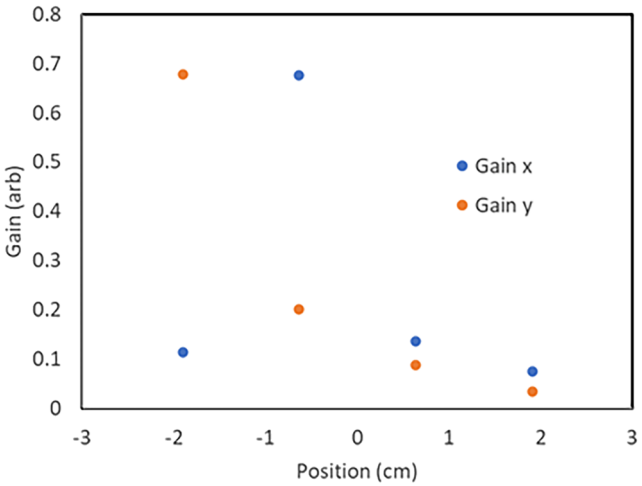

FIG. 8. Profile monitor channel sensitivities measured for pRad0942, which were used to normalize inconsistencies between the channels.

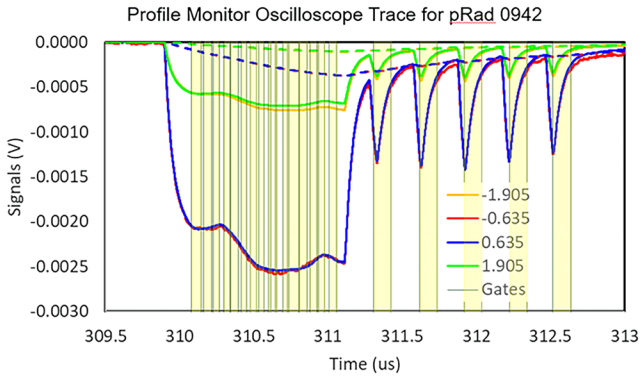

FIG. 9. Sensitivity corrected profile monitor traces from a typical run in this analysis. The integration gates corresponding to each of the camera gates for each of the 21 pulses are shown by the light gray lines and shaded yellow. The signal (solid line) and tail correction (dashed line) for each channel are plotted. The blue and red traces represent the innermost fibers, while the yellow and green traces represent the two outermost fibers. Changes in the relative voltage obtained from the fibers from pulse to pulse show beam movement between pictures.

and the corresponding standard deviations were computed. The integration gates shown in Fig. 9 were adjusted by up to 40 ns on a frame-by-frame basis to minimize the standard deviation between the predicted and measured beam positions. A plot of the predicted vs measured quantities is shown in Fig. 10, and the standard deviations of the fitted quantities compared to the initial values are provided in Table I.

The rms beam width is about 1 cm for this experiment, and the beam jitters about +/− 1 mm. The beam shifts result in slopes in ratio images, which are $\frac{dR}{dx} = \frac{x}{\sigma^2}$, where x is the position and σ is the beam width. These starting beam shifts lead to 5%–10% variations in the ratios of images (such as dynamic vs beam) across the central part of the image. After correcting with profile monitor data, these are reduced by a factor of 6 in the y direction and 12 in the x direction. This makes absolute 1% radiography, as in uncertainties in transmission are less than 1%, possible.

VI. TRANSMISSION AND AREAL DENSITY COMPUTATION

The aim of the beam profile monitor is to improve the accuracy of the transmission and areal density data obtained, which is the primary motivation behind most experiments at pRad.

The interaction of protons with matter for pRad can be approximately described by three interactions: the nuclear interaction; the Coulomb interaction with the electrons in matter that results in continuous energy loss; and the Coulomb interaction with nuclei that results in Gaussian scattering.[1]

Contrast in the image is generated by a collimator that cuts the scattering angles resulting from Coulomb multiple scattering of the protons as they transit the object. Transmission is given by the product of nuclear scattering and Coulomb scattering,[1]

$$N(x,y) = N_0(x,y)e^{-\frac{\rho_A(x,y)}{\lambda}}\left(1 - e - \frac{\theta^2_{collimator}}{2\theta^2_{scatter}(x,y)}\right), \quad (2)$$

$$\theta_{scatter} = \frac{14.1}{p\beta}\sqrt{\frac{\rho_A(x,y)}{X_0}}.$$

Here, $N_0(x,y)$ is the incident beam and a function of coordinates x and y, $N(x,y)$ is the transmitted beam, $\rho_A(x,y)$ is the areal density the beam encounters, β is the beam velocity relative to the speed of light, p is the beam momentum in units of MeV/c, X_0 is

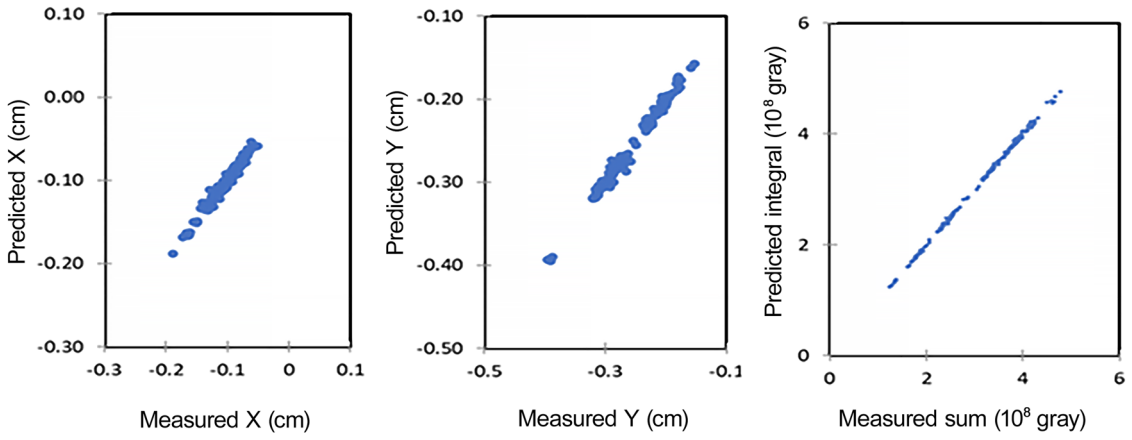

FIG. 10. Plots of predicted beam centroids and integrals vs measured beam centroids and integrals, which were used to obtain the standard deviations shown in Table I.

TABLE I. Standard deviations of the fits to eight beam images giving 128 images.

	SD starting	SD fitted
x	248 μm	41 μm
y	516 μm	40 μm
Sum	29.7%	0.69%

the radiation length of the material, and λ is the nuclear scattering length. Inverting this expression to find $\rho_A(x,y)$ requires knowledge of $N_0(x,y)$.[1]

The areal density can be described as the volumetric density integrated with respect to the z direction, as shown in the following equation:

$$\rho_A(x,y) = \int \rho_V(x,y,z)dz. \tag{3}$$

The areal densities can be computed from the transmission images by inverting,

$$T(x,y) = \frac{N(x,y)}{N_0(x,y)}, \tag{4}$$

where λ and X_0 are known. This expression assumes a single material and no background. However, the images can be corrected for background if its level is known, which can be measured using a shadow bar at the upstream image location. Shadow bar measurements were used in previous pRad analysis.[11] While this has not been done here, it should be explored for future experiments.

The nuclear attenuation length was taken from previous step wedge fits to a range of materials. There is ambiguity between the collimator angle and the radiation length for the material, so we have obtained X_0 by fitting the transmission from the static image. The fit shown in Fig. 11 results in X_0 given in Table II. The values for fixed radiation lengths were estimated using shot drawings.

The parameters have been used to invert the transmission measurements for each image of the dynamic sequence using Eqs. (2) and (4). The final results of the analysis are shown in Fig. 12.

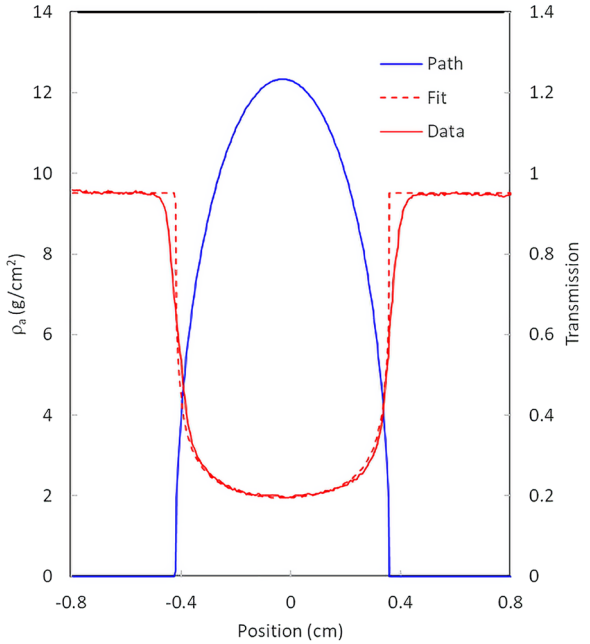

FIG. 11. Fit (red dashed line) to a lineout through the static transmission (red solid line). The model of the object is shown as the blue line.

TABLE II. Parameters used for the result in 10.

Radius	0.390 0 cm
Fixed RL	0.050 0
x_0	7.458 9 g/cm^2
λ_0	74.524 8 g/cm^2
ρ	15.6 g/cm^3
θ_{fixed}	0.002 6 rad
Collimator	0.010 0

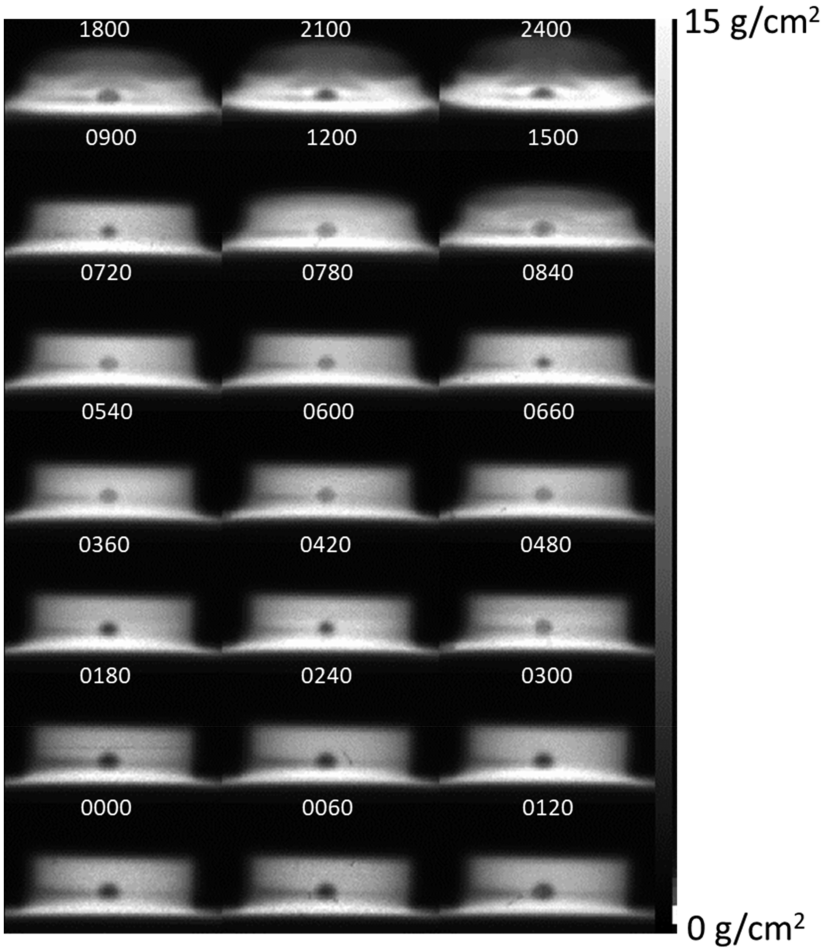

FIG. 12. The areal density sequence for pRad0942. Time progresses from left to right and bottom to top. The time (in nanoseconds) after the first frame is labeled in the plot.

VII. CONCLUSIONS

The beam profile monitor provides in situ quantitative information about the beam intensity, position, and width on a pulse-by-pulse basis. This information can be used to normalize radiographs for changes in the beam between pictures. The precision of the position information is 40 μm and of the intensity information is 0.7%. Implementing the analysis technique presented here allows absolute measurements of transmission with less than 1% error across the pRad field of view with no need for less reliable methods of flattening, a new capability for pRad at LANSCE. Future work on the beam profile monitor aims to reduce the inconsistencies in signal between channels utilizing a new design that will eliminate the need for epoxy, allowing for swapping out damaged fibers as needed.

ACKNOWLEDGMENTS

This work was supported by the U.S. Department of Energy through the Los Alamos National Laboratory, which is operated by Triad National Security, LLC, for the National Nuclear Security Administration of U.S. Department of Energy (Contract No. 89233218CNA000001).

AUTHOR DECLARATIONS

Conflict of Interest

The authors have no conflicts to disclose.

Author Contributions

All authors contributed equally to this work.

Lauren O'Brien: Conceptualization (equal); Data curation (equal); Formal analysis (equal); Investigation (equal); Methodology (equal); Resources (equal); Validation (equal); Visualization (equal); Writing – original draft (equal); Writing – review & editing (equal). **Gerrit Bruhaug**: Data curation (equal); Writing – review & editing (equal). **Jeremy Danielson**: Data curation (equal); Methodology (equal); Validation (equal); Visualization (equal); Writing – review & editing (equal). **Skylar Farmer**: Data curation (equal); Investigation (equal); Validation (equal); Writing – review & editing (equal). **Saryu Fensin**: Data curation (equal); Writing – review & editing (equal). **Matt Freeman**: Data curation (equal); Validation (equal); Writing – review & editing (equal). **Matthew Fresquez**:

Data curation (equal); Writing – review & editing (equal). **Drew Hall**: Data curation (equal); Writing – review & editing (equal). **Anna Llobet**: Data curation (equal); Writing – review & editing (equal). **Fesseha Mariam**: Conceptualization (equal); Data curation (equal); Methodology (equal); Writing – review & editing (equal). **Israel Martinez**: Data curation (equal); Writing – review & editing (equal). **Erin Mavis**: Data curation (equal); Writing – review & editing (equal). **Jason Medina**: Data curation (equal); Writing – review & editing (equal). **Wil Meijer**: Conceptualization (equal); Data curation (equal); Investigation (equal); Methodology (equal); Resources (equal); Validation (equal); Visualization (equal); Writing – review & editing (equal). **Levi Neukirch**: Conceptualization (equal); Data curation (equal); Investigation (equal); Methodology (equal); Resources (equal); Validation (equal); Visualization (equal); Writing – review & editing (equal). **Steven Sandoval**: Data curation (equal); Methodology (equal); Resources (equal); Writing – review & editing (equal). **Mary Sandstrom**: Data curation (equal); Funding acquisition (equal); Writing – review & editing (equal). **John Schmidt**: Data curation (equal); Writing – review & editing (equal). **Erick Smith**: Conceptualization (equal); Data curation (equal); Methodology (equal); Writing – review & editing (equal). **Zhaowen Tang**: Conceptualization (equal); Data curation (equal); Formal analysis (equal); Investigation (equal); Methodology (equal); Resources (equal); Validation (equal); Visualization (equal); Writing – review & editing (equal). **Carl Trujillo**: Data curation (equal); Writing – review & editing (equal). **James Wernicke**: Data curation (equal); Writing – review & editing (equal). **Brandon White**: Data curation (equal); Methodology (equal); Resources (equal); Writing – review & editing (equal). **Christopher L. Morris**: Conceptualization (equal); Data curation (equal); Formal analysis (equal); Investigation (equal); Methodology (equal); Resources (equal); Software (equal); Supervision (equal); Validation (equal); Visualization (equal); Writing – original draft (equal); Writing – review & editing (equal).

DATA AVAILABILITY

The data that support the findings of this study are available from the corresponding author upon reasonable request.

REFERENCES

[1] C. L. Morris, N. S. P. King, K. Kwiatkowski, F. G. Mariam, F. E. Merrill, and A. Saunders, "Charged particle radiography," Rep. Prog. Phys. **76**(4), 046301 (2013).

[2] K. Hanson and U. Schneider, "History of proton radiography and tomography," Z. Med. Phys. **32**(1), 2–4 (2022).

[3] G. E. Hogan, K. J. Adams, K. R. Alrick, J. F. Amann, J. G. Boissevain, M. L. Crow, S. B. Cushing, J. C. Eddelman, C. J. Espinoza, T. T. Fife *et al.*, "Proton radiography," in *Proceedings of the IEEE Particle Accelerator Conference* (IEEE, 1999).

[4] N. S. P. King, E. Ables, K. Adams, K. R. Alrick, J. F. Amann, S. Balzar, P. D. BarnesJr, M. L. Crow, S. B. Cushing, J. C. Eddleman *et al.*, "An 800-MeV proton radiography facility for dynamic experiments," Nucl. Instrum. Methods Phys. Res., Sect. A **424**(1), 84–91 (1999).

[5] W. Buttler, D. M. Oro, D. L. Preston, K. O. Mikaelian, F. J. Cherne, R. S. Hixson, F. G. Mariam, C. Morris, J. B. Stone, G. Terrones *et al.*, "Unstable Richtmyer–Meshkov growth of solid and liquid metals in vacuum," J. Fluid Mech. **703**, 60–84 (2012).

[6] E. N. Ferm, S. Dennison, R. Lopez, K. Prestridge, J. Quintana, C. Espinoza, G. Hogan, N. King, J. Lopez, F. Merrill *et al.*, "Proton radiography experiments on shocked high explosive products," AIP Conf. Proc. **706**, 839–842 (2004).

[7] D. Holtkamp, D. A. Clark, E. N. Ferm, R. A. Gallegos, D. Hammon, W. F. Hemsing, G. E. Hogan, V. H. Holmes, N. S. P. King, R. Liljestrand *et al.*, "A survey of high explosive-induced damage and spall in selected metals using proton radiography," AIP Conf. Proc. **706**, 477–482 (2004).

[8] L. Smilowitz, B. F. Henson, D. Remelius, P. Bowlan, N. Suvorova, J. Allison, D. Cardon, M. Freeman, F. Mariam, W. Meijer *et al.*, "Experimental observations of exploding bridgewire detonator function," J. Appl. Phys. **128**(21), 215901 (2020).

[9] L. Smilowitz, B. F. Henson, J. J. Romero, B. W. Asay, A. Saunders, F. E. Merrill, C. L. Morris, K. Kwiatkowski, G. Grim, F. Mariam *et al.*, "The evolution of solid density within a thermal explosion II. Dynamic proton radiography of cracking and solid consumption by burning," J. Appl. Phys. **111**, 103516 (2012).

[10] G. Terrones, M. W. Burkett, and C. L. Morris, "Burn front and reflected shock wave visualization in an inertially confined detonation of high explosive," AIP Conf. Proc. **1426**, 239–242 (2012).

[11] C. L. Morris, E. Ables, K. R. Alrick, M. B. Aufderheide, P. D. Barnes, Jr., K. L. Buescher, D. J. Cagliostro, D. A. Clark, D. J. Clark, C. J. Espinoza *et al.*, "Flash radiography with 24 GeV/c protons," J. Appl. Phys. **109**(10), 104905 (2011).

[12] C. T. Mottershead and J. D. Zumbro, "Magnetic optics for proton radiography," Proc. Part. Accel. Conf. **2**, 1397–1399 (1998).

[13] H. A. Bethe, "Molière's theory of multiple scattering," Phys. Rev. **89**(6), 1256 (1953).

[14] V. Douence, Y. Bai, H. Durmus, A. B. Joshi, P. Pettersson, D. Sahoo, K. Kwiatkowski, N. S. P. King, C. Morris, M. D. Wilke *et al.*, "Hybrid image sensor with multiple on-chip frame storage for ultra high-speed imaging," Proc. SPIE-Int. Soc. Opt. Eng. **5580**, 226–234 (2005).